Revista Mexicana de Astronomía y Astrofísica, **32**, 75–87 (1996)

THE SPATIAL INTENSITY DISTRIBUTION OF THE UV LIGHT IN HH OBJECTS. REVISITED

A. Moro-Martin[1], A. Noriega-Crespo[1,2], K.-H. Böhm[3], and A.C. Raga[4]

Received 1996 March 26; accepted 1996 May 30

RESUMEN

Muchas de las características observadas en objetos Herbig-Haro han podido ser reproducidas mediante modelos de choque de proa. Se muestra que modelos similares pueden usarse para la distribución espacial de intensidad de las líneas ultravioleta observadas por *IUE*. Se han utilizado espectros del archivo de *IUE* para estudiar las líneas ultravioleta (C IV λ1549, Si III] λ1891, C III] λ1909, C II] λ2326, Mg II λ2799) y también el continuo (modelado como continuo de dos fotones de hidrógeno), de los objetos: HH 1, HH 2(H+A′), HH 2(G+B), HH 24A, HH 32A, HH 43(A+B+C) y HH 47A. Los datos de *IUE* tienen un calidad limitada, debido a lo amplio de su función de ensanchamiento de punto y su baja señal a ruido; por tanto los modelos han sido degradados para compararlos con las observaciones. Los parámetros físicos de los modelos se basan en estudios ópticos anteriores y fueron variados dentro de sus intervalos de incertidumbre para reproducir las observaciones. Los objetos se modelaron como un único choque de proa (i.e., HH 1, HH 24A, HH 32A y HH 47A) o la superposición de dos (i.e., HH 2(H+A′) y HH 2(G+B)) o más (i.e., HH 43(A+B+C)). La idea es tomar en cuenta la compleja estructura de estos objetos y la contribución a la luz ultravioleta de otras condensaciones dentro del apertura de *IUE*.

ABSTRACT

Simple kinematical bow shock models have successfully explained many of the observed features in Herbig-Haro objects. It is shown that similar models can be applied to the spatial intensity distribution of the UV lines observed by *IUE*. Archival *IUE* spectra have been used for the HH 1, HH 2(H+A′), HH 2(G+B), HH 24A, HH 32A, HH 43(A+B+C), and HH 47A objects, where the brightest UV lines (C IV λ1549, Si III λ1891, C III] λ1909, C II] λ2326, Mg II λ2799) were studied, as well as the UV continuum (modeled by the hydrogen two-photon continuum). The quality of the *IUE* data is rather limited due to the broad point spread function and the low signal-to-noise, and therefore the models were degraded to make them comparable to the observations. The physical parameters used in the models were obtained from previous optical studies and varied accordingly to match the observations, but within the known uncertainties. The objects were modeled by a single bow shock model (i.e., HH 1, HH 24A, HH 32A, and HH 47A) or the superposition of two (i.e., HH 2(H+A′) and HH 2(G+B) or more (i.e., HH 43(A+B+C)) of them. The idea was to take into account the complexity of the morphology of these objects, and the contribution to the UV light from different condensations within the *IUE* aperture.

Key words: **ISM — JETS AND OUTFLOWS**

[1] Maria Mitchell Observatory, USA.
[2] Infrared Processing and Analysis Center, USA.
[3] University of Washington, USA.
[4] Instituto de Astronomía, UNAM, México.

1. INTRODUCTION

Herbig-Haro (HH) objects are diffuse emitting regions associated with the supersonic gas outflow from young stellar objects (YSOs). A large fraction of their UV, optical and near infrared emission is in the form of permitted (e.g., Hα, C IV) and forbidden (e.g., [S II], [Fe II]) lines, which arise in the recombination region of the shock excited gas (Schwartz 1975), a consequence of their supersonic interaction with the surrounding medium. The HH condensations in many cases resemble morphologically working surfaces, which are characterized by two shocks, the Mach disk (or jet shock) and the bow shock (e.g., Hartigan 1989; Raga 1989). In detail, however, their structure is more complex, as ground (Eislöffel, Mundt, & Böhm 1994) and *HST images* (Hester et al. 1994) have recently revealed.

Several of the intrinsic properties of such HH objects, e.g., intensity line ratios, position-velocity diagrams, velocity dispersion and their optical *spatial intensity distribution* (hereafter SID), have been modeled in a reasonable way by simple kinematical bow shock models. The success of the models relies on the following reasons. First, that for most objects the Mach and bow shock are too close to be spatially resolved. Second, that the geometry of the bow shock allows the simultaneous presence of strong (at is apex) and weak (at its wings) shocks. Finally, that for the gas densities which have been estimated for the jet and the surroundings (Raga & Noriega-Crespo 1993), the emission of the bow shock dominates over that of the Mach disk (Hartigan 1989; Raga 1989).

HH objects display a wide range of emission line excitations in the UV, from C IV λ1549 to Mg II λ2799, which can be easily explained in the context of a bow shock structure. In a curved shock it is only the perpendicular component of the shock velocity which becomes thermalized, this makes possible to have high excitation lines near the apex and low excitation ones arising from the wings of a bow shock (see, e.g., Böhm 1990; Brugel 1989).

The goal of this paper is to compare the SID of the UV light observed in HH objects with those predicted by kinematical bow shock models. Although a comparison between the *IUE* data and 'degraded' optical observations has been previously carried out by Lee et al. (1988), the comparison with the shock models should provide a more clear understanding of the physical conditions in HH objects. The *IUE* data has been collected from the published literature (Lee et al. 1988; Böhm et al. 1987; Böhm, Scott, & Solf 1991; Böhm et al. 1992; Böhm, Noriega-Crespo, & Solf 1993) The objects studied are HH 1, HH 2, HH 24A, HH 32, HH 43, and HH 47, with a

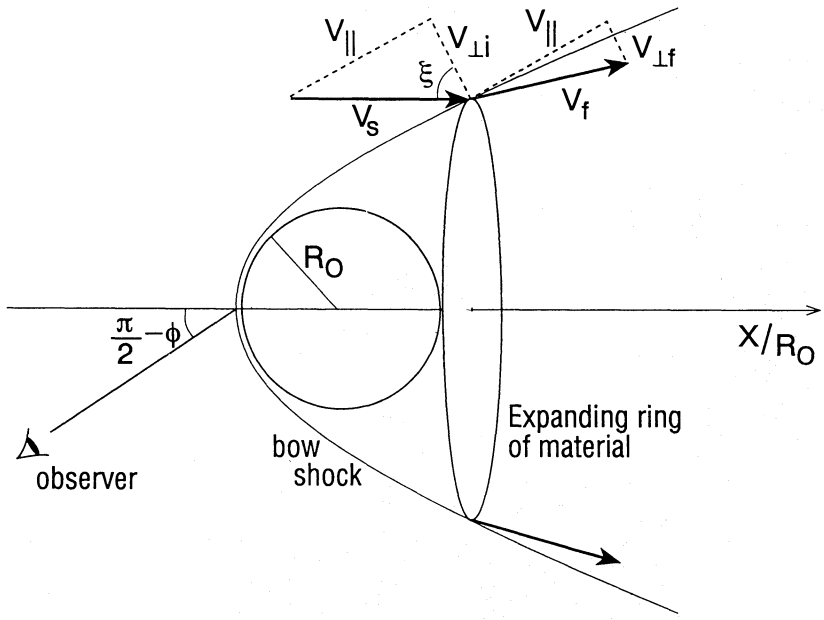

Fig. 1. Bow shock geometry. The gas enters the bow shock at a velocity V_S and at an angle ξ. The parallel component of the velocity ($V_{\|}$) is conserved across the shock, while the perpendicular component is thermalized (from $V_{\perp i}$ to $V_{\perp f}$). The angle between the plane of the sky and the symmetry axis of the bow shock is ϕ. The bow shock models are created by using a spherical obstacle of radius R_0.

particular attention to their stronger emission lines: C IV λ1549, C III] λ1909, Mg II λ2799, Si III] λ1891 (if available), and the continuum.

The properties and limitations of the kinematical bow shock models are described in § 2. The discussion of the theoretical SIDs and their assumptions are included in § 3. The comparison with individual HH objects is presented in § 4, and our concluding remarks in § 5.

It is shown, as suspected from the optical observations (Eislöffel et al. 1994; Hester et al. 1994) and model position-velocity diagrams (Indebetouw & Noriega-Crespo 1995) that the match between theory and observations improves when the presence of multiple condensations is considered in their interpretation.

2. THE KINEMATICAL BOW SHOCK MODEL

2.1. Geometry

A detailed description of a simplified bow shock model can be found, for instance, in Hartigan, Raymond, & Hartmann 1987 (hereafter HRH87). The idea is that the emission of a bow shock can be modeled by the superimposed emission produced by individual plane parallel shocks along its surface. The intensity (velocity) of each shock depends only on its position on the surface. To illustrate this consider a gas flow entering the bow shock with a velocity V_S at angle ξ (see Figure 1). For a given orientation of the bow shock surface (ϕ), the parallel ($V_\parallel$) and perpendicular ($V_\perp$) components of the velocity can be calculated at each point. Since it is only ($V_\perp$) which becomes thermalized, this is the velocity associated with the plane shock. In practice to obtain the emission along the surface, the bow shock is subdivided into a number of annuli. The intensity from each annulus is determined by running a plane parallel shock model with velocity equal to its corresponding $V_\perp$. This emission is then weighted by the area of the annulus and co-added with that arising from the rest of the annuli. This process produces the line emission from the entire bow shock. For a given line the SID is obtained by integrating the emission along the line of sight. The final distribution is convolved with a Gaussian with a width given by the point-spread function (PSF) of the instrument. The *IUE* PSF is between 4″ and 5″, depending on the wavelength (see, e.g., de Boer & Meade 1981). The models are then normalized to the size of the object (R_0), so that the resulting distributions are scale-free, and to the peak intensity value (I_0).

The planar shock models, which provide the value of the intensity as a function of shock velocity, come from HRH87 and have been interpolated to be mapped smoothly onto the bow shock model (see Figure 2*a*). A careful interpolation is particularly important for the low velocity shocks which have an important contribution to the intensity over the large surface area of the bow shock wings. An example of this can be seen in the intensity distribution of Mg II λ2799, where both interpolation and grid resolution 'conspire' as to generate some noise at the wings (see Figure 2*b*). In most cases the grid size of N = 500 elements was enough to minimize the noise.

2.2. The Grid of Models

Prior to the comparison between the observed SIDs and the corresponding theoretical distributions, we ran a series of models to understand their general properties. For a given line the characteristics of the plane parallel shock models (i.e., HRH87) plus the geometry of the bow shock are what determine the shape of the SID. A grid of models was created by considering the following parameters: (1) the shock velocity (100, 150, 200, 250 km s^{-1}), (2) the angle between the bow shock axis and the plane of the sky (0°, 30°), (3) the preshock density (100, 1000 cm^{-3}), and (4) the preshock ionization state of the gas. Both fully and equilibrium preionized gas models were considered (see HRH87). The preionization structure in a bow shock can be more complex (see e.g., Raymond, Hartigan, & Hartmann 1988), but for the optical lines equilibrium models seem to match better the observations (Noriega-Crespo, Böhm, & Raga 1989).

As examples of the SID directly obtained from the bow shock models, i.e., without convolving with the *IUE* PSF, the models for the lines C IV λ1549 and Mg II λ2799 are presented in Figure 2*b* (in equilibrium and fully ionized for n = 100 cm^{-3} and ϕ = 0°). These two lines were chosen because they show the overall behavior that is seen in the high and low excitation lines. Notice that difference between the spatial distributions can be traced back to those already present in the shock models of each line (Figure 2*a*). For example, the small 'bumps' in the fully preionized shock models for the Mg II λ2799 line, become amplified by the extent of the emitting area of the bow shock wings in the SID.

Some general features that can be identified from the grid of models are the following: (1) The emitting region gets wider as the shock velocity increases. In fact the full width at the zero intensity level for a low excitation line is approximately equal to the shock velocity (HRH87). (2) The preionization state affects the spatial distribution of the emission lines. A fully ionized model gives different and wider distribution than an equilibrium one. In an ionized gas the energy released by the shock is not used for further ionization. This permits weak shocks along the bow shock wings to contribute to the emission. (3) As the 'viewing angle' or inclination (angle between the bow axis and the plane of the sky), ϕ, increases the profiles become smoother, which it is expected from the geometry of the bow shock. (4) Some structure seen

at a few radii from the stagnation region in the distributions is due to a combination of the 'coarseness' of the geometrical grid with the finite interpolation of the plane parallel models.

2.3. Limitations of the Model

Some important limitations of the bow shock model described above are the following: (1) The preshock ionization state is not well known: the preshock material entering a certain annulus is not only being ionized by the photons coming from this annulus but also by the ones next to it. Bow shock models including this effect (Raymond et al. 1988) seem to reproduce the observed line intensities and ratios. (2) Planar shock models are not reliable in the low velocity range. This fact, together with the projection problems arising when using high orientation angles (ϕ) and integration intervals larger than 7 R_0, make it difficult to model low excitation HH objects, as HH 43, where the shock velocities are relatively low. (3) The model assumes a uniform density medium, which is not always thought to be the case. Preshock density is not well known. (4) HH objects present more complex structures than the single, double and triple condensation models studied in this paper. (5) The model does not take into account emission from the Mach disk and the jet itself. Thermal instabilities are neglected, as well as molecular cooling.

3. THE SPATIAL INTENSITY DISTRIBUTIONS

3.1. General Remarks

We focused on the study of the strongest UV lines, C IV λ1549, Si III] λ1891, C III] λ1909, and Mg II λ2799, as well as on wide bands of continuum emission. Table 1 contains a summary of the spectral images that were used for this study including the object, number, exposure time and year of observation (columns 1 through 4 respectively). The labels correspond to the long (LW) or short (SW) wavelength spectrographs and to the prime (P) and redundant (R) cameras, e.g., LWR13004 refers to the long wavelength spectra number 13004 taken with the redundant camera. The LW camera in the low dispersion mode covers from 1860 to 3300 Å and the SW camera in the same mode covers from 1150 to 1975 Å. Columns (5) and (6) refer to the orientation of the slit in the observations and the models. For an overview of the basic technical details of the *IUE* satellite operation, which includes how to obtain and reduce the data see, e.g., Harris & Sonneborn (1987).

It has been pointed out several times the limitations of *IUE* for the study of HH objects (see, e.g., review by Böhm 1990), nevertheless is one of the few instruments that have provided us with simultaneous information of the spatial and spectral properties of these objects at ultraviolet wavelengths. The main caveats to study the HH objects SIDs are due to (1) their relatively low surface brightness, (2) the fact that they are found in star forming regions which are not necessarily transparent to the UV light, and (3) the limited spatial resolution due to *IUE*'s broad PSF.

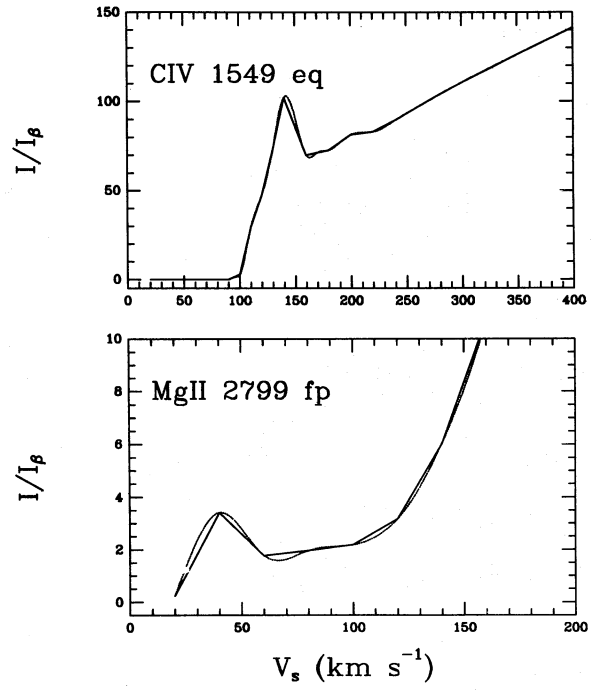

Fig. 2. (*a*) A sample of the plane parallel shock models used to obtain the spatial intensity distributions (SID). The models give the intensity radiated (normalized with respect to Hβ) as a function of the shock velocity for the C IV λ1549 and Mg II λ2799 lines. The models can be computed in equilibrium (eq) or full ionization (fp) of the preshock gas. The solid line are the values from HRH87 and the broken line the interpolation used.

To deal with these problems, we have concentrated on the shape of the *normalized* intensity distribution for a given line, avoiding reddening corrections. We have performed also a convolution of the models with the *IUE* PSF to avoid deconvolving the observations, which it is proven to be more difficult and less reliable (see, e.g., Lee et al. 1988). The *IUE* PSF varies as a function of wavelength, and so it was taken as a Gaussian with a FWHM of 4″, for the C IV and Mg II lines and 5″ for C III], Si III] and the continuum (de Boer & Meade 1981). Since the size for many of these objects, from the ground at optical wavelengths, are $\sim$ 5″ most of the spatial details are lost in the convolution. If the size of the UV emitting region, however, is *larger* than 5″, then the compar-

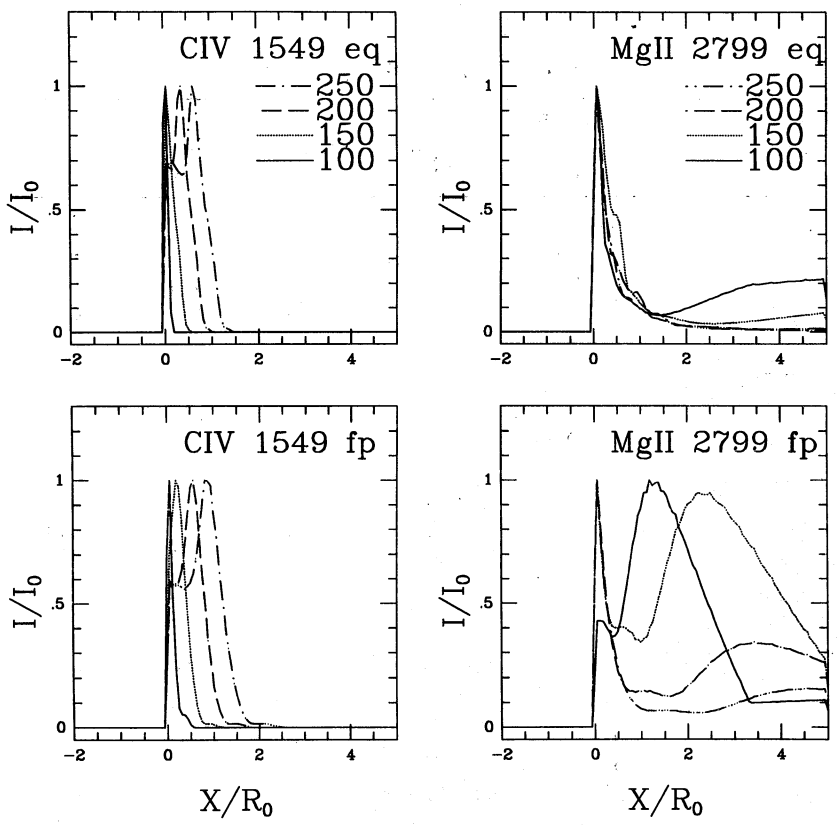

Fig. 2. (*b*) A sample of the SIDs created by the kinematical bow shock model for the high excitation C IV λ1549 and the low excitation Mg II λ2799 emission lines. The models correspond to a set of shock velocities of 100, 150, 200, 250 km s^{-1}, at the two different initial gas preionizations.

ison with the models as well as their interpretation becomes very interesting (see below). The models have been shifted to match the peak intensity distribution of the most reliable observed line. Once this is done the relative shift for all the other comparison lines, for the same exposure, is identical.

A final caveat when comparing the models with the HH objects *IUE* observations is due to the lack of "error bars" in the published data. For the brightest objects like HH 1 and HH 2 a typical estimate of the uncertainties in the fluxes is ∼ 10%–15%. For fainter objects like HH 43, HH 47 and specially HH 24 the uncertainties in their calibrated fluxes can be larger. In this study we are interested in the spatial distribution of the flux integrated over a wavelength interval. This is less uncertain than the monochromatic flux. In HH 24 for instance (the faintest object of our sample), the spatial dependence of the integrated spectra can be fairly reliably determined by making the comparison of 2 different *IUE* measurements (see, e.g., Fig. 6 in Böhm et al. 1992).

3.2. SID Model Assumptions

The physical parameters for the models were obtained from ground-based optical studies. The initial parameter space was based on the best available shock velocities, proper motions, radial velocities and optical spectra. In some cases the input numbers for the models were varied within the known uncertainties, although, as previously pointed out, it is difficult to try to constrain theoretical models completely using *IUE* observations.

The kinematical bow shock model assumes that a spherical obstacle gives raise to the bow shock. This radius has been identified (historically) with the (half) size of the brightest region of the bow shock-like HH object, as e.g., ∼ 4″(2″) in HH 1F (Eislöffel et al. 1994). In view that most of theses objects correspond in reality to a working surface driven by a jet, then it is possible to interpret the diameter of the obstacle as an upper limit to the width of the jet.

For all the models, given the wide aperture of *IUE*

TABLE 1

ARCHIVAL *IUE* SPECTRAL DATA

Object Name (1)	Image No. (2)	Exposure Time (min) (3)	Year Observed (4)	Observed PA(°) (5)	Model PA(°) (6)
HH 1	SWP 8188	270	1980	337	330
	SWP16668	270	1982	348	330
	SWP24914	729	1985	303	330
	SWP40657	633	1991	315	330
	LWR 8912	134	1980	167	145
HH 2(H+A′)	SWP10218	270	1980	165	145
	SWP10246	290	1980	167	145
	SWP16671	430	1982	349	330
	SWP18157	430	1982	167	145
	SWP24919	860	1985	304	330
	SWP40663	675	1991	312	330
	LWR 8888	180	1980	165	145
	LWR 8909	150	1980	167	145
	LWR10450	380	1981	5	330
HH 2G	SWP43891	636	1992	315	330
HH 24A	SWP21518	560	1983	189	155
	SWP22708	485	1984	153	155
	SWP38033	680	1990	307	335
	SWP38102	585	1990	320	335
	LWP 3140	120	1984	153	155
HH 32A	LWR13004	414	1982	261	285
HH 43	SWP17522	390	1982	132	145
	SWP23749	425	1984	147	145
	SWP24924	580	1985	304	335
	SWP31828	781	1987	159	145
	LWP 4041	420	1984	146	145
HH 47A	SWP17549	400	1982	78	55
	SWP21389	440	1983	168	135
	SWP32154	411	1987	128	135
	SWP33960	870	1988	340	355

($\sim 10'' \times 23''$), we have taken a slit with a width 10 times the radius of the bow shock. The theoretical slit was set along the position angle of the inferred direction of the outflow, which was determined using ground-based images of [S II] and Hα. This corresponds to a difference of $\sim 2°$ to $\sim 30°$ with respect the position of *IUE* slit (see Table 1). For the 'degraded' SIDs we found that these differences were not important as is the case, for instance, in the position-velocity diagrams of the optical lines (see, e.g., Raga & Böhm 1986).

For condensations like HH 2(H+A′) or HH 43 (A+B+C), where a superposition of bow shock models was used, we proceeded as follows to combine the models. (1) A model for the brightest condensation was generated, (2) a second or third model were created and scaled in flux and size using the initial brightest condensation model for the normalization, and (3) these later models were shifted accordingly to their corresponding relative distances and then co-added.

The models which resemble more the observations were those calculated under the assumption of equilibrium preionization. Fully preionized and equilibrium plane shock models are identical for shock velocities above 180 km s^{-1} (HRH87). The difference arises at low velocities, which manifest themselves along the bow shock wings. Because of this, the low

velocity shocks control the extent and shape of the 'tails' in the SIDs, particularly for the low excitation lines. So with the exception of HH 32A (see Table 2) the peak velocity of the HH objects considered lies below the 180 km s^{-1} threshold, and therefore, both equilibrium and fully ionized models were calculated. The later ones, however, do not match as well the observations, except perhaps for HH 32A (see below). A similar conclusion was reached by Noriega-Crespo et al. (1989) with respect to the optical forbidden lines.

The main focus of this study is the shape of the SIDs, although for consistency the integrated fluxes of the models and the observations were also compared. The fluxes match within factors of 2 and 10, except for the two photon continuum where the factors are higher, a direct consequence from the fact that the plane parallel shock models overestimated the two photon continuum flux (HRH87).

In Table 2 we summarized the parameters of the bow shock models for the objects (column 1) studied. These are the shock velocity, viewing angle and size (columns 2 through 4, respectively).

TABLE 2

PARAMETERS FOR THE BOW SHOCK MODELS[a]

Object	V_S (km s^{-1})	ϕ (°)	Diameter (″)
(1)	(2)	(3)	(4)
HH 1	175	5	4.0
HH 2A′	170	12	3.4[b]
	...	...	3.6[c]
	...	...	5.6[d]
HH 2H	125	2	5.0[b]
	...	...	4.8[c]
	...	...	3.0[d]
HH 2G	110	−5	1.8
HH 2B	105	2	0.8
HH 24A	50	−36	6.0
	100	−36	6.0
HH 43A	100	60	4.6
HH 43B	40	55	5.0
HH 32A	300	70	5.0[e]
HH 43C	35	75	3.6
HH 47A	100	23	6.4

[a] Most models are in equilibrium preionization.
[b] Position angle = 5°.
[c] Position angle = 165°, 349°.
[d] Position angle = 304°, 312°.
[e] Fully preionized.

4. DISCUSSION ON INDIVIDUAL OBJECTS

4.1. HH 1

HH 1 is a high-excitation object and one of the brightest in the ultraviolet (together with HH 2). We have modeled it as a single condensation with a shock velocity of 175 km s^{-1}, an inclination $\phi = 5°$ (moving into the plane of the sky), a preshock density of 100 cm^{-3}, and a radius $R_0 = 2''$. Figure 3 shows a comparison between the *IUE* observations and the models for 2 selected emission lines: C IV λ1549 and Si III] λ1891, and two 200 Å wide continuum bands, 1500−1700 and 1700−1900 Å. These models assume equilibrium pre-ionization. In Figure 3 (as in the rest of the figures) the broken line represents the *IUE* PSF and the solid line the convolution of the model with the PSF.

It is interesting to notice that the *IUE* observations are in this case wider than the PSF, which suggests that the condensation was resolved (but see below). The single condensation models are just slightly wider than the PSF, but not as much as the observations. This would seem to indicate that the UV emission is not limited to only the stagnation zone, where the shock is completely thermalized, but it is more extended. This is a bit surprising for the C IV and Si III] lines, since it is expected that their emission arises from the 'apex' where enough energy is available for their excitation after the thermalization of relatively fast shock waves. On the other hand the C IV λ1549 distribution for SWP24914 is at the half maximum $\sim 20 - 25\%$ wider than the model. The Si III] λ1891 has to be considered with some caution because at the spectral resolution of *IUE* it is partially blended with C III λ1909. The observed shapes of the SIDs are themselves quite different from a Gaussian PSF, something which becomes more evident when looking at the continuum emission. Only in the case of the C IV λ1549 from the SWP24914 exposure, the observed distribution has a comparable extent as the model. Notice that the corresponding SID from the SWP40657 exposure, which was taken at a similar orientation looks broader. Some of the remaining differences between models and observations in the case of HH 1 (and probably for the rest of the objects too) could be due to a more complex morphology and preionization state of the gas.

4.2. HH 2 (H+A′) and HH 2 (G+B)

The HH 2 object, which is the southern bipolar counterpart of HH 1, has a high excitation and a very complex structure (see, e.g., Eislöffel et al. 1994; Schwartz et al. 1993; Hester et al. 1994).

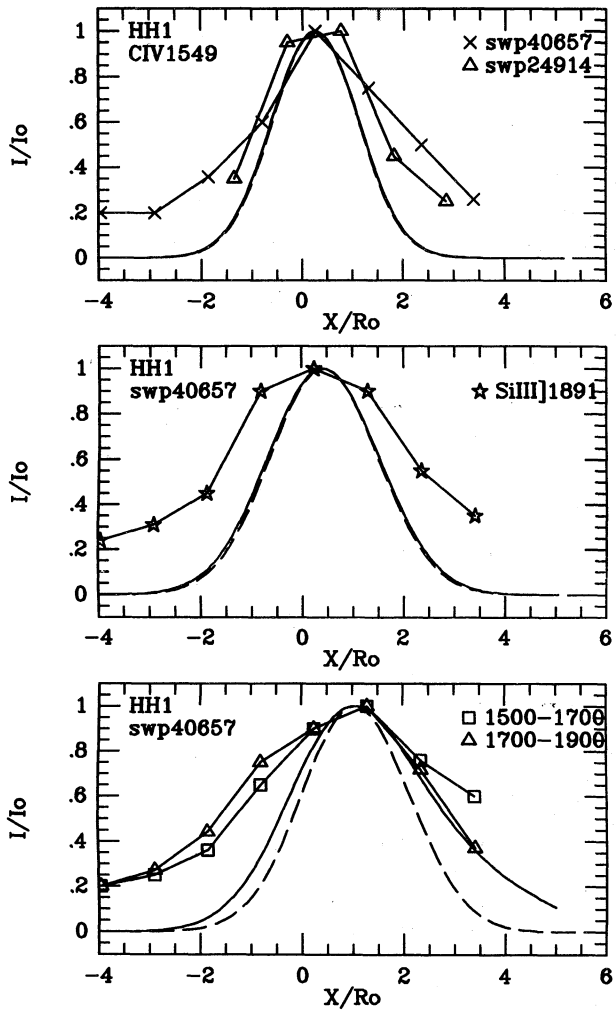

Fig. 3. Comparison of the observed and theoretical spatial intensity distributions of HH 1, for the C IV λ1549 and the Si III] λ1891 lines and two continuum bands 200 Å wide. The solid line corresponds to the convolution of the model with the *IUE* point spread function (broken line).

We modeled HH 2 (H+A′) as the superposition of two bow shock models with a preshock density of 100 cm^{-3} and equilibrium pre-ionization. The shock velocity and inclination used to model HH 2H and HH 2A′ were 125 km s^{-1}, 2°, and 170 km s^{-1}, 12° respectively (following Indebetouw & Noriega-Crespo 1995), with both objects moving into the plane of the sky.

Since from ground base observations HH 2H alone displays an almost elliptical shape, we considered in the models a minimum and maximum value for its size depending on the location of the *IUE* aperture (see Table 2). Recall that the models assume a spherical obstacle for the formation of the bow shock. The separation between HH 2H and HH 2A′ varies with the slit orientation as well, an effect also included in the models. In practice these are minor adjustments to the resulting SIDs, since it is the superposition of two bow shocks models what determines the SID shape. The radii for HH 2H, HH 2A′ and their separation were determined from the FWHM of images taken by 2 meter-like telescopes in [S II] and Hα (Lee et al. 1988; Böhm et al. 1991; Böhm & Solf 1990).

Observationally (see Figures 4*a,b*), the distributions for the C IV and C III] lines in the SWP18157 and SWP40663 frames are wider than the point spread function (broken line). This was the first indication of contribution of more than one condensation to the UV light. The superimposed double bow shock model does a very good job in matching the extent of the SWP40663 lines (Figure 4*a*). The 'hump' of the model distribution suggests that the double peak structure that is observed is for real and not an artifact of the *IUE* observations. At a different orientation for the SWP18157 frame, the superimposed model resembles that of the observations both in shape and extent.

There is another condensation that has been observed in HH 2: HH 2G. The optical images suggest that HH 2G emission may have a contribution from HH 2B within the *IUE* aperture, so once again we tried the superposition of two bow shock models. HH 2B is a small condensation and its size was determined using some 3.5-m sub-arcsecond images (Reipurth et al. 1993). Recall that the models use the radius of the object, but in practice what it is measured is the FWHM size of a condensation and this is taken as its diameter (see Table 2).

The models that better match the observations assume a radius $R_0 = 0.9''$ for HH 2G and 0.4″ for HH 2B and a distance between condensations of 2.8″(see Figure 4*c*). Equilibrium preionization and a 100 cm^{-3} preshock density were used. The shock velocities and the angles between the axis and the plane of the sky were derived from the proper motions (Eislöffel et al. 1994) and the radial velocities (Böhm et al. 1992). Although both objects are essentially in the plane of the sky, we use −5° for HH 2G (moving towards the observer) and 2° for HH 2B (moving into the sky). In practice the distributions do not depend on these values. The *HST* images tentatively indicate the presence of [O III] in HH 2B (Hester et al. 1994), which suggests shock velocities of ∼ 100 km s^{-1}. In the models, therefore, velocities of this order were considered. The models in Figure 4*c* correspond to 110 km s^{-1} for HH 2G and 105 km s^{-1} for HH 2B. The observed distributions of the C IV and C III] lines for SWP43891 (Böhm et al. 1993) are again broader than the PSF. The model for C IV at the half intensity maximum is narrower than the observations by ∼ 45%, ahead of the main shock (negative values of X/R_0). The superimposed double

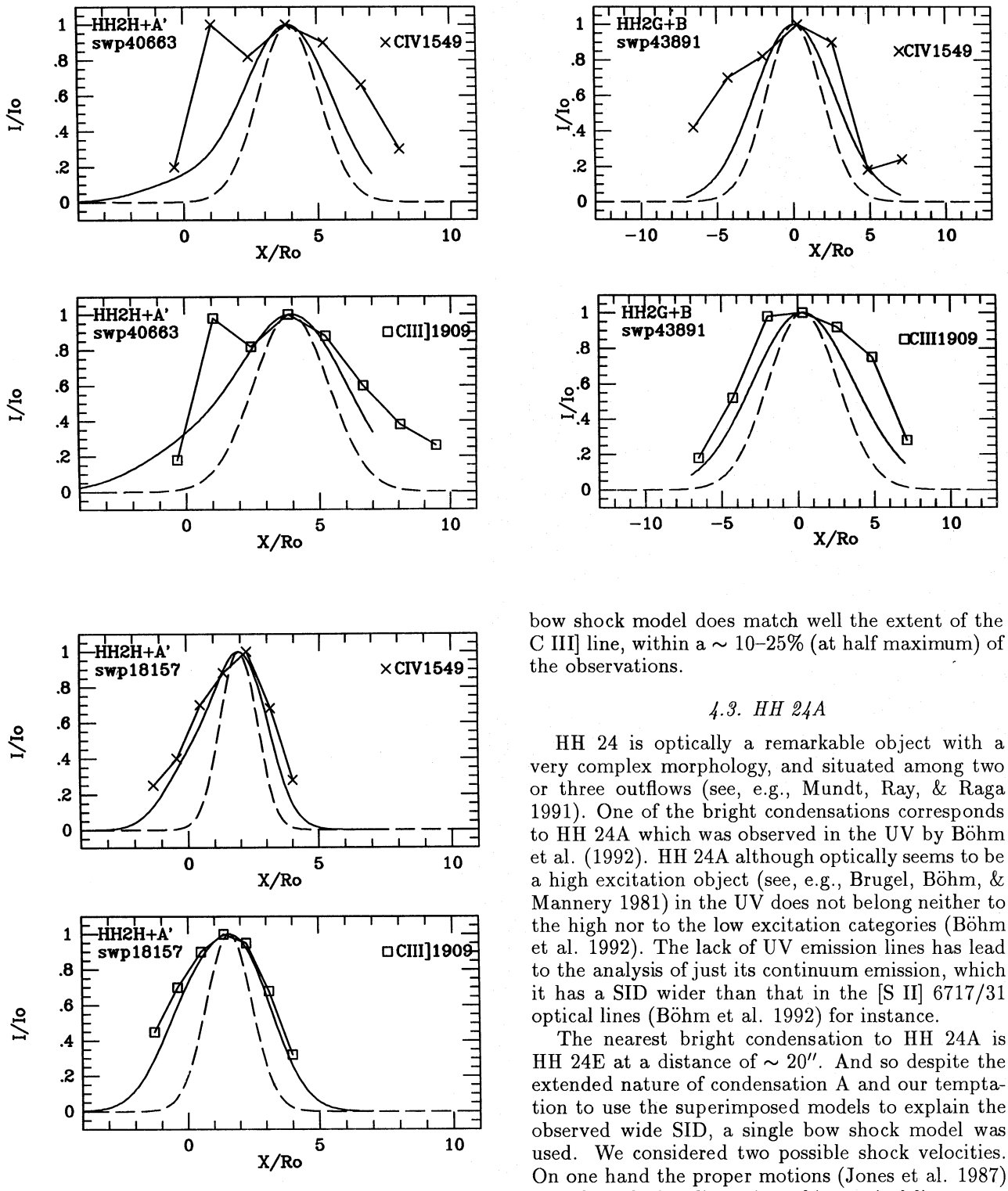

Fig. 4. As in Figure 3, but for the HH 2(H+A′) condensations in the C IV λ1549 and C III] λ1909 lines for two different *IUE* observations (*a*) SWP40663 and (*b*) SWP18157 (see Table 1) using the superposition of two bow shock models. (*c*) The distributions for the same lines but for the HH 2(G+B) condensations.

bow shock model does match well the extent of the C III] line, within a ∼ 10–25% (at half maximum) of the observations.

4.3. HH 24A

HH 24 is optically a remarkable object with a very complex morphology, and situated among two or three outflows (see, e.g., Mundt, Ray, & Raga 1991). One of the bright condensations corresponds to HH 24A which was observed in the UV by Böhm et al. (1992). HH 24A although optically seems to be a high excitation object (see, e.g., Brugel, Böhm, & Mannery 1981) in the UV does not belong neither to the high nor to the low excitation categories (Böhm et al. 1992). The lack of UV emission lines has lead to the analysis of just its continuum emission, which it has a SID wider than that in the [S II] 6717/31 optical lines (Böhm et al. 1992) for instance.

The nearest bright condensation to HH 24A is HH 24E at a distance of ∼ 20″. And so despite the extended nature of condensation A and our temptation to use the superimposed models to explain the observed wide SID, a single bow shock model was used. We considered two possible shock velocities. On one hand the proper motions (Jones et al. 1987) and the velocity dispersion of its optical lines, e.g., Hα, [N II] λ6583 and [S II] λ6731 (Solf 1987), suggests a shock velocity relatively low ∼ 50 km s^{-1}. On the other hand the detection of [O III] λ5007 (Brugel et al. 1981) implies a shock velocity of ∼ 100 km s^{-1}. Both bow shock models (for 50 and 100 km s^{-1}) as-

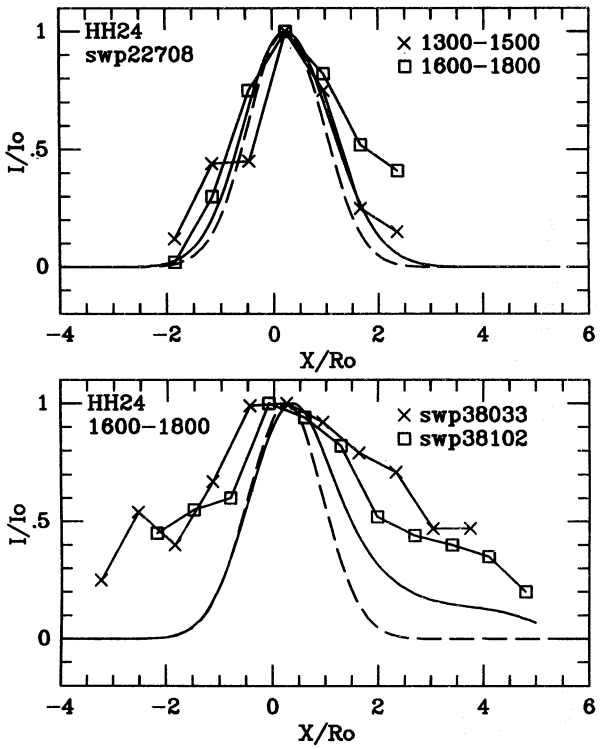

Fig. 5. As in Figure 3, but for the continuum distributions at 1300–1500 Å and 1600–1800 Å for HH 24A. The observations correspond to different position angles (see Table 1). The SWP22708 distributions (top) are compared with a V_{shock} = 50 km s^{-1} model. The SWP38033/102 distributions (bottom) with a V_{shock} = 100 km s^{-1} model (see text).

sume equilibrium preionization with a preshock density of 100 cm^{-3}, a radius of 3″ and an angle of −36° (towards the observer).

In Figure 5 we show the comparison with the observations of two different 200 Å wide continuum bands, 1300–1500 Å and 1600–1800 Å. The top panel corresponds to the 50 km s^{-1} model and the bottom one to the 100 km s^{-1} model. The comparison with the SWP22708, at a position angle of 153° with the 50 km s^{-1} bow shock model looks very good. Both observation and model are hardly wider than the PSF. The SWP38033 and SWP38102 observations were taken at similar position angle of 307° and 320° respectively, but ∼ 150° apart from the SWP22708 position (see Table 1). For this set of observations the 100 km s^{-1} model resembles the observed distribution more closely, although the observations are a lot more extended at negative values of X/R_0. In HH 24 it is possible that the *IUE* observations have mapped two different velocity regions (∼ 50–100 km s^{-1}) with the two different aperture positions. Some of remaining differences could be due to the relative faintness of HH 24 and the large uncertainties in determining its fluxes. The broadening of the SID could arise during the extraction of the fluxes in the 'outskirts' of the line-by-line spectra, where it is difficult to set the zero intensity level and there is a tendency to overestimate the measured flux in low signal-to-noise regions (Böhm et al. 1992).

4.4. HH 32A

From the ground-based observations HH 32 can be characterized by three bright condensations (see, e.g., Hartigan, Mundt, & Stocke 1986; Davis, Eislöffel, & Smith 1996). Condensation A is optically the brightest with a complex morphology and the one studied by *IUE*. HH 32A displays a high excitation (see, e.g., Hartigan et al. 1986) with a strong [O III] λ5007 emission and also a high extinction with an $E(B-V) \sim 0.6$ (see, e.g., Brugel et al. 1981).

The only *IUE* data available is for the Mg II λ2799 line, due to the strong effect of the extinction at smaller wavelengths (Lee et al. 1988). We consider a bow shock model at an inclination angle with respect the plane of the sky of 70° (Solf, Böhm, & Raga 1986), which agrees well with more recent estimates (e.g., 60° by Davis et al. 1996). Based on the mentioned spectroscopic data and radial velocity measurements plus HH 32A proper motions (Herbig & Jones 1983), we selected a shock velocity of 300 km s^{-1}. A preshock density of 100 cm^{-3} and a radius of $R_0 = 2.5''$ were used. Models at both preionizations were calculated, but in this case the fully ionized model shown in Figure 6, resembles more closely the observed SIDs. Indeed for LWR13004 at the half maximum both model and observation are essentially identical. The difference appears at fainter intensity levels along the 'tail' of the distribution, i.e., positive values of X/R_0 (see Fig. 6).

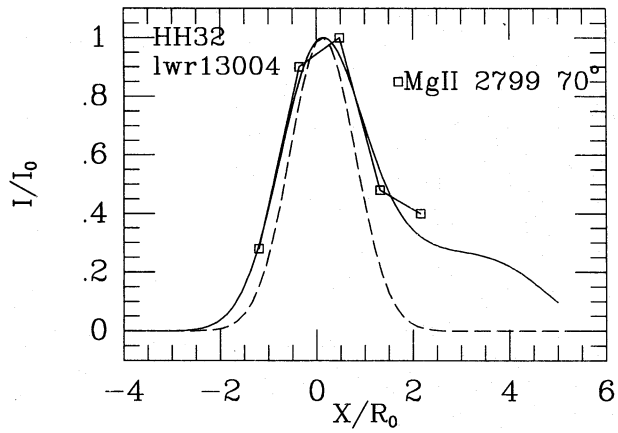

Fig. 6. As in figure 3, but for the Mg II λ2799 line in HH 32A. The model corresponds to an inclination with respect to the plane of the sky of 70° and a 300 km s^{-1} shock velocity.

4.5. HH 43 and HH 47A

Both HH 43 and HH 47A are low excitation objects, with spectral features from fluorescent H_2 emission and UV continuum (Böhm et al. 1991). A systematic grid of plane parallel shock models for H_2 does not exist, and therefore we used shock models of the 2-photon continuum emission of hydrogen for both objects (see below). In Figures 7 and 8 we show the SIDs for HH 43 and HH 47A, respectively, for the SWP24924, LWP4041, SWP31828 and SWP33960 observations.

The HH 43 system was modeled as a triple condensation (A+B+C) with a preshock density of 100 cm^{-3} and equilibrium preionization for each condensation. From the analysis of the data presented by Schwartz, Dopita, & Cohen (1985), HH 43A was modeled with a shock velocity of 100 km s^{-1} at an inclination angle of 60° into the sky. For HH 43B and HH 43C the values used were 40 km s^{-1} at 55°, and 35 km s^{-1} at 75° respectively (Indebetouw & Noriega-Crespo 1995). The approximate sizes of the condensations were derived from the position-velocity diagrams in Böhm & Solf (1990) and are given in Table 2. The distances between condensations depend on the position angle of the slit. For the HH 43A/43B and 43B/43C pairs their distances are 5.5″/6.9″, 6.9″/6.9″ and 6.6″/7.5″ for the 304°, 159° and 146° position angles, respectively.

The observed SIDs are wider than the PSF by almost a factor two. The SIDs are so wide that even the 3 condensations models do not match exactly their extent. The models, nevertheless, trace the correct trend of a more extended 'wing' emission from the UV continuum. Recall that the plane parallel shock models, which are input in the bow shock models, are relatively uncertain at low velocities (~ 20–30 km s^{-1}) and no models are available below these values. This is crucial for the bow shock models with a peak shock velocity of ~ 35–40 km s^{-1} at a relatively large inclination, since this has the tendency to enhance the emission from the 'wings'. In addition there is a serious possibility (see, e.g., Böhm, et al. 1991) that at least in the 1400–1600 Å wavelength range the continuum emission is strongly influenced by the H_2 continuum emission which shows a different spatial distribution from the 2-photon hydrogen continuum.

The HH 47A object is one of the four main bow shocks observed in the remarkable HH 46–HH 47 system in the Gum Nebula (see, e.g., Eislöffel & Mundt 1994). It is a low excitation object, with clear spectral features of fluorescent H_2 emission and continuum (Böhm et al. 1991). The input parameters for the model SID are a 100 km s^{-1} shock velocity, equilibrium preionization, a preshock density of 100 cm^{-3}, an inclination angle of 23° (into the plane of the sky) and a radius of ~ 3.2″ (Raga et al. 1987).

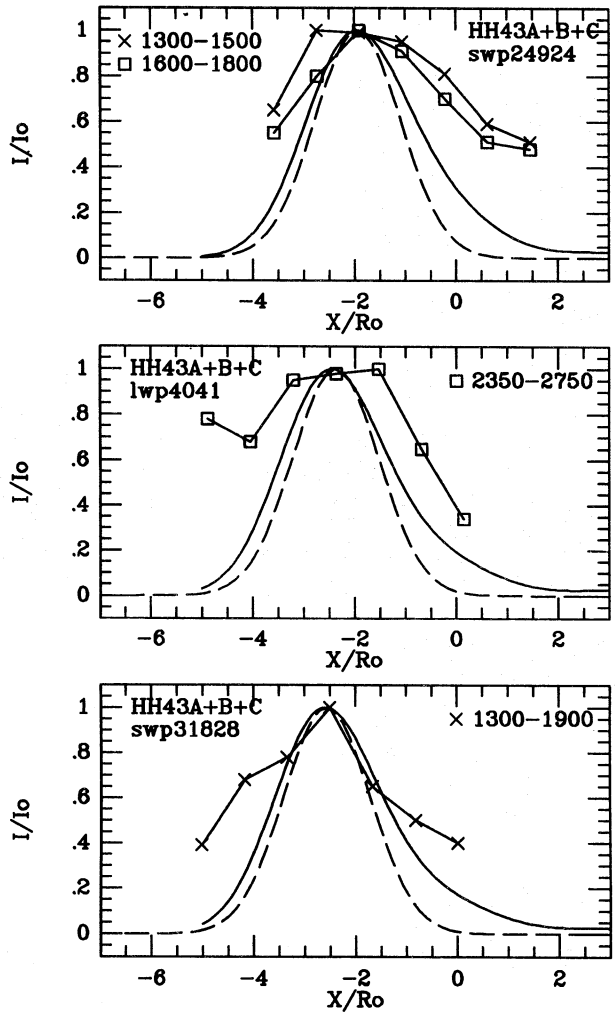

Fig. 7. As in Figure 3, but for the HH 43(A+B+C) system and a triple condensation model and three different continuum observations: 200 (top), 400 (center) and 600 Å (bottom) wide, respectively.

Observationally the continuum at 1300–1900 Å (Figure 8) is almost twice as wide as the PSF (Böhm et al. 1991). In this case, however, a single condensation model seems to reproduce the observations, including the 'tail' of the SID. Perhaps the most surprising thing about HH 47A is that a shock velocity of 100 km s^{-1} works for a low excitation object. A similar conclusion was reached by Curiel et al. (1995) based on their analysis of the GHRS and FOC *HST* observations, which led them to invoke a more complex shock structure, where C-type magnetic shocks or a MHD precursor may be present.

CONCLUSIONS

The goal of this study has been to use a simple kinematical model to understand and revisit the spa-

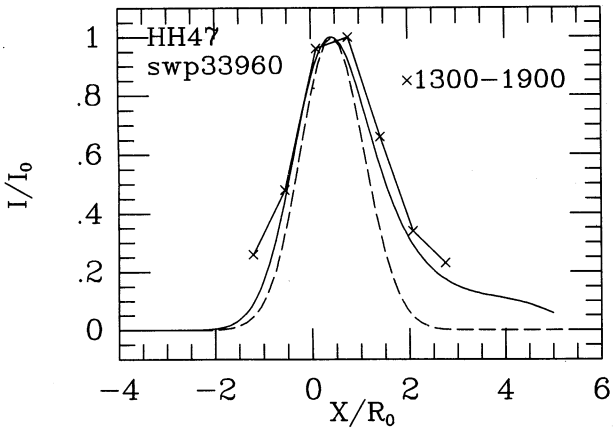

Fig. 8. As in Figure 3, but for the 600 Å wide continuum distribution of HH 47A.

tial intensity distributions observed in the UV light by *IUE* of some HH objects. The SID models overall have shown that many of the parameters that have been obtained by optical means provide a self-consistent picture when used to explain the UV emission. The models presented here stress the basic idea that to reproduce the emission from these objects it is necessary to include the contribution to radiation from most of their brighter condensations.

The superposition of two or three bow shocks to mimic the contribution to the UV light seems to match better the observations. This is particularly the case for HH 2(H+A′), HH 2(G+B), and HH 43(A+B+C). Some of the remaining differences between models and observations could be due to a more complex preionization structure (see, e.g., Raymond et al. 1988). This process determines in part the emission ahead and behind the bow shock. For the low velocity shocks a higher preionization allows them to emit farther into the bow shock wings creating wider SIDs. Perhaps this is the case for HH 43 and HH 47A which require relatively low velocities to understand their spectra. For these objects the uncertainty of their fluxes and the plane shock models at those velocities, coupled with their large viewing angles, makes the comparison with the models less compelling. Also, for these low excitation objects there may be additional continuous emission processes (H_2?) which have not been incorporated into the models.

For HH 24A to explain the observed SIDs at two different aperture positions seem to require single bow shock models at two different shock velocities. This can be understood if the *IUE* observations at those apertures were indeed mapping two distinct velocity regions of a working surface. For HH 24A and HH 43(A+B+C) some of the differences could be have been enhanced by the different position angles that were used (see Table 1). Changes in the shape of the SID due to a different position angle manifest themselves at the tail of the distribution (positive values of X/R_0). In the comparison, however, the interesting differences seem to take place ahead of the main shock (negative values of X/R_0). Finally, for HH 32A a single bow shock model with a large inclination (70°) and high shock velocity (300 km s^{-1}) reproduces quite well the observed SID.

It is a pleasure to thank E. Friel for her support and helpful comments, and the referee for her/his suggestions. A.M-M. was supported by a Perkin Fellowship during her stay at MMO. A.N.-C. research is supported by NASA Long Term Astrophysics Program through JPL under contract with Caltech, and NSF grant AST9300391 through MMO.

REFERENCES

Böhm, K.-H. 1990, in Evolution in Astrophysics, *IUE* Astromomy in the Era of New Space Missions, ESA Conf. Proc. SP-310, 23
Böhm, K.-H., & Solf, J. 1990, ApJ, 348, 297
Böhm, K.-H., Noriega-Crespo, A., & Solf, J. 1993, ApJ, 416, 647
Böhm, K.-H., Scott, D.M., & Solf, J. 1991, ApJ, 371, 248
Böhm, K.-H., Noriega-Crespo, A., Solf, J., & Brugel, E.W. 1992, PASP, 104, 251
Böhm, K.-H., Buhrke, Th., Raga, A.C., Brugel, E.W., Witt, A.N., & Mundt, R. 1987, ApJ, 316, 349
Brugel, E.W. 1989, in Low Mass Star Formation and Pre-Main Sequence Objects, ed. B. Reipurth, ESO Conference and Workshop Proceedings, 33, 311
Brugel, E.W., Böhm, K.H., & Mannery, E. 1981, ApJS, 47, 117
de Boer, K.S., & Meade, M.R. 1981, NASA *IUE* Newsletter 15, 53
Curiel, S., Raymond, J.C., Wolfire, M., Hartigan, P., Schwartz, R.D., & Nisenson, P. 1995, ApJ, 453, 322
Davis, C.J., Eislöffel, J., & Smith, M.D. 1996, ApJ, in press
Eislöffel, J., & Mundt, R. 1994, A&A, 284, 530
Eislöffel, J., Mundt, R., & Böhm, K.-H. 1994, AJ, 108, 1042
Harris, A.W., & Sonneborn, G. 1987 in Exploring the Universe with the *IUE* Satellite, ed. Y. Kondo, 729
Hartigan, P. 1989, ApJ, 339, 987
Hartigan, P., Mundt, R., & Stocke, J. 1986, AJ, 91, 1357
Hartigan, P., Raymond, J., & Hartmann, L. 1987, ApJ, 316, 323
Herbig, G., & Jones, B.F. 1983, AJ, 88, 1040
Hester, J.J., Scowen, P.A., Lynds, R., & O'Neil, E.J. 1994, BAAS, 26, 1386
Indebetouw, R., & Noriega-Crespo, A. 1995, AJ, 109, 752
Jones, B.F, Cohen, M., Wehinger, P.A., & Gehren, T. 1987, AJ, 94, 1260
Lee, M.G., Böhm, K.-H., Temple, S.D., Raga, A.C., Mateo, M.L., Brugel, E.W., & Mundt, R. 1988 AJ, 96, 1690

Noriega-Crespo, A., Böhm, K.-H., & Raga, A.C. 1989, AJ, 98, 1388
Mundt, R., Ray, T.P., & Raga, A.C. 1991, A&A, 252, 740
Raga, A.C. 1989, AJ, 98, 976
Raga, A.C., & Böhm, K.-H. 1986, 308, 829
Raga, A.C., & Noriega-Crespo, A. 1993, RevMexAA, 25, 149
Raymond, J.C, Hartigan, P., & Hartmann, L. 1988, ApJ, 326, 323
Reipurth, B., Heathcote, S., Roth, M., Noriega-Crespo, A., & Raga, A.C. 1993, ApJ, L49
Schwartz, R.D. 1975 ApJ, 195, 631
Schwartz, R.D., Dopita, M.A., & Cohen, M. 1985, AJ, 90, 820
Schwartz, R.D., Cohen, M., Jones, B.F., Böhm, K.-H., Raymond, J.C., Hartmann, L.W., Mundt, R., Dopita, M. & Schultz, A.S.B. 1993, AJ, 106, 740
Solf, J. 1987, A&A, 184, 322
Solf, J., Böhm K.-H., & Raga, A.C. 1986, ApJ, 305, 795

Karl-Heinz Böhm: Dept. of Astronomy FM-20, University of Washington, Seattle, WA 98195 USA. (bohm@astro.washington.edu).
Amaya Moro-Martin: Maria Mitchell Observatory, Nantucket, MA 02554 USA. (mamoro@mmo.org).
Alberto Noriega-Crespo: Infrared Processing and Analysis Center, 100–22, 7705 Wilson Av., Pasadena, CA 91109-8099 USA. (alberto@ipac.caltech.edu).
Alejandro C. Raga: Instituto de Astronomía, UNAM, Apartado Postal 70-264, 04510 México, D.F., México. (raga@astroscu.unam.mx).